

Supplementary Information

More versatility than thought: large {Zr₂₆} oxocarboxylate cluster by corner-sharing of standard octahedral subunits

Bahareh Nateghi,^a Ishtvan Boldog,^{*a} Konstantin V. Domasevitch,^b Christoph Janiak^{**a}

^a Institute of Inorganic Chemistry and Structural Chemistry, Heinrich-Heine-Universität Düsseldorf, Universitätsstr. 1, D-40225 Düsseldorf, Germany. E-mail: ishtvan.boldog@gmail.com, janiak@uni-duesseldorf.de

^b Inorganic Chemistry Department, Taras Shevchenko National University of Kiev, Vladimirskaya Street 64, Kiev 01033, Ukraine

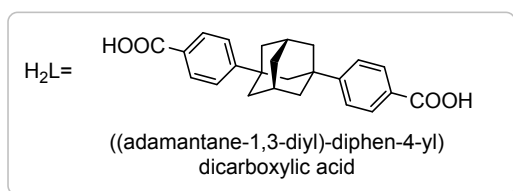
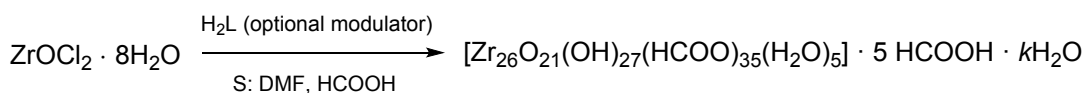
E-mail: ishtvan.boldog@gmail.com, janiak@uni-duesseldorf.de

Contents

1. Synthesis	1
2. Single crystal X-ray diffraction structure determination	3
3. PXRD	9
4. TGA.....	11
5. FT-IR spectroscopy	13
6. ¹ H NMR spectrum of 1 after digestion	14
7. Gas adsorption studies.....	15

1. Synthesis

Materials. ZrOCl₂ · 8H₂O (99%, Sigma-Aldrich), N,N-dimethylformamide (DMF; 99.8%, Sigma-Aldrich), formic acid (99%, Sigma-Aldrich), deionized water. The ((adamantane-1,3-diyl)-diphen-4-yl) dicarboxylic acid (H₂L) was synthesized according to the literature [1].



Scheme. S1.

Synthesis of 1: 42.5 mg (132 μmol) of $\text{ZrOCl}_2 \cdot 8\text{H}_2\text{O}$ were dissolved in 7.28 ml DMF after prolonged shaking until formation of a clear solution with, possibly, a very small amount of insoluble residues (Scheme 1). Addition and dissolution of 12.4 mg (33 μmol) of H_2L was followed. Finally, 4.56 mL (121 μmol) of formic acid was added. The mixture was thoroughly mixed and sealed in a 20 ml culture tube. The sealed tube was heated for 4 days at 140 $^\circ\text{C}$. The formed white deposit, composed of small needle-like crystals, was filtered off, washed with a few small portions of DMF and left drying in air on a Petri dish until constant weight. Yield of the white microcrystalline material was 16 mg (~14%). The used high dilution was seemingly necessary for sufficient purity and crystallinity of the product (including the suitability of monocrystals for SCXRD). The addition of H_2L seemed to have only one important effect: it increased the single-crystal sizes slightly, which allowed the SCXRD studies. Otherwise, there is no need for its use.

The scaled-up experiments were performed analogously, but without the addition of H_2L , using 5.8 \times times of the initial quantities in a 250 ml hermetic vessel (Caution! The vessel is pressurized during the synthesis due to partial decomposition of the formic acid. It is advisable to leave a significant overhead space, up to $\frac{1}{2}$ of the flask's volume. Large scale experiments, typically in vessels that has comparably lower pressure resistance, pose more risk compared to the small scale ones). The results of IR, PXRD measurements and the adsorption studies are given for the samples obtained in scaled-up syntheses.

Elemental analysis for $[\text{Zr}_{26}\text{O}_{21}(\text{OH})_{27}(\text{HCOO})_{35}(\text{H}_2\text{O})_5] \cdot 5 \text{HCOOH} \cdot k\text{H}_2\text{O} \cdot l\text{DMF}$:

calcd (%) for $\text{C}_{40}\text{H}_{86}\text{O}_{135}\text{Zr}_{26}$ ($k = 2, l = 0$; conforms with the TGA): C 9.42, H 1.70

calcd (%) for $\text{C}_{40}\text{H}_{102}\text{O}_{143}\text{Zr}_{26}$ ($k = 10, l = 0$; conforms with the SCXRD): C 9.16, H 1.96

calcd (%):for $\text{C}_{61}\text{H}_{151}\text{N}_7\text{O}_{150}\text{Zr}_{26}$ ($k = 10, l = 7$; best conformance with the elemental analysis): C 12.73, H 2.64, N 1.70

found (%): C 12.35, H 2.63, N 1.74

Notes. the elemental analysis was performed on sample from a repeated large scale synthesis. The sample for the analysis was not dried to constant weight to avoid the loss of the solvent of crystallization. A small amount of sample was, rather, pressed between filter-papers, then dried for a short time in air, until no aggregation of the particles, characteristic for a wet sample was observed. The sample was then sealed in a hermetic vial and stored in it until the analysis.

The short time drying allowed to avoid significant loss of solvent, but it has the drawback of incomplete removal of the surface adsorbed / interparticle solvent. The result of the analysis witnesses a presence of significant amount of DMF (and, most probably, a commensurate amount of formic acid, however with low impact on elemental analysis data in the latter case). Fortunately, either the analysis of the residual peaks in the pre-SQUEEZED SCXRD structure (see p. 2) and, especially, the ^1H NMR spectrum of a digested sample, which was washed by acetone, shows no significant presence of DMF inside the crystals and hence in was not added to the final formula.

In any case, the results are considered to be satisfactory, given the possible presence of other phases as admixtures (see PXRD) and the relatively low sensitivity of elemental analysis due to low content of organics.

2. Single crystal X-ray diffraction structure determination

The single crystals of **1** could be best described as thin elongated wedge-shaped blocks (Fig. S1). A thin 'blade' end of suitable optical quality was cut-off for the measurement. The diffraction data were collected on a Stoe STADIVARI diffractometer with a Dectris Pilatus 300K detector and with a Cu microfocus source (Cu-K α , $\lambda = 1.54186 \text{ \AA}$) at 180(2) K using a nitrogen gas open-flow cooler Cobra from Oxford Cryosystems. Data reduction and cell refinement were processed using X-Area [2]. Face-indexed numerical absorption correction using X-RED and X-SHAPE [3] was applied. The structure was solved by direct methods and refined by full-matrix least-squares on F^2 using the programs SHELXS-97 and SHELXL-2014/7 [4]. The information regarding data collection and structure refinement is summarized in Table S1.

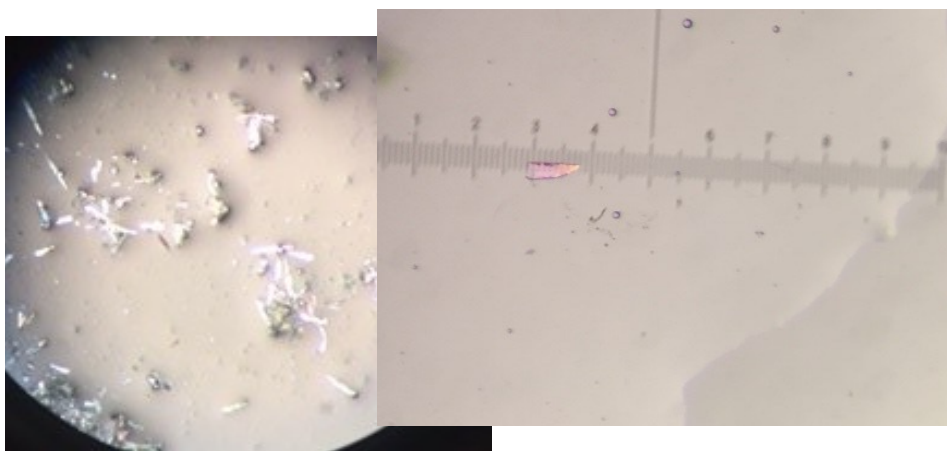


Fig. S1. Micrographs of the crystals of **1**.

Refinement details.

All non-hydrogen atoms belonging to the cluster were refined in anisotropic model, while the atoms of the solvate formic acid molecules in isotropic. The (C)H hydrogen atoms of the formates / formic acid molecules were placed geometrically and refined in a riding model, $U_{\text{iso}}(\text{H}) = 1.2U_{\text{eq}}(\text{CH})$. The (O)H hydrogen atoms were not placed explicitly (see below).

The structure of the cluster features two major problems: a) the site-sharing of the $\text{H}_2\text{O}/\text{HCOO}^-$ ligands and b) the correct assignment of the $\mu_3\text{-O}^2/\mu_3\text{-OH}^-$ ligands.

The first problem becomes evident after careful examination of the atomic thermal motion parameters and residual electron densities, which shows features characteristic for disorder both on the periphery of the cluster and in the solvate regions. Large thermal displacement parameters of the formate ligands referenced further by their C6 and C7 atoms, which are bridging the Zr3, Zr5 and Zr5, Zr4 atoms respectively, and the residual peaks at 2.10-2.21 \AA from the Zr ions suggests partial occupancies of the formate groups and presence of two aqua ligands as the second site-sharing components (Fig. S2). The $\mu\text{-COO}^- / 2\text{H}_2\text{O}$ site-sharing was resolved smoothly with partial occupancies of 0.60 / 0.40 for O35-C6-O36 / (O3w, O4w) components and 0.40 / 0.60 for O37-C7-O38 / (O1w, O2w) ones. A similar monodentate $\text{HCOO}^- / \text{H}_2\text{O}$ site-sharing with 0.5/0.5 ratio of components was observed at the Zr11 ion. Additionally, all the three monodentate formate groups exhibit

disorder of carbon atoms, which were refined with fixed partial occupancies set to make their thermal parameters approximately equal.

The possible $\mu_3\text{-O}^{2-}/\mu_3\text{-OH}^-$ site-sharing is expected from the chemical composition and is confirmed by the high anisotropy of the thermal motion for some of the $\mu_3\text{-O}$ atoms (O17 to O20). Although the positions of the hydrogen atoms belonging to $\mu\text{-OH}$ were not located, the assignment of the hydroxo- and oxo-ligands within the cluster was possible in view of subtle coordination features. All four unique μ -oxygen atoms (O21 to O24) represents the bridging hydroxo ligands with Zr-O bond length in the range of 2.140(2)-2.199(5) Å and Zr-O-Zr bond angle in the range of 108.4(2)-111.5(2)°. These values perfectly match the corresponding parameters for the similar moieties in the known crystal structure of $[\text{Zr}_6(\mu_3\text{-O})_4(\mu_3\text{-OH})_4](\mu\text{-OH})_4[\text{Zr}_6(\mu_3\text{-O})_4(\mu_3\text{-OH})_4]$, Zr-O 2.159 Å and Zr-O-Zr 111.5°, where the dodecanuclear units are integrated further by dicarboxylate ligands in a polymer [5].

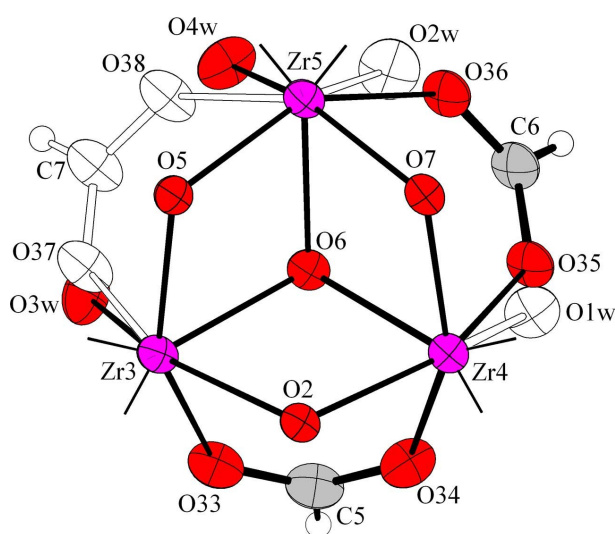


Fig. S2. The site-sharing scheme for the formate and aqua ligands coordinated to the Zr₃, Zr₄ and Zr₅ atoms. The O₃₅-C₆-O₃₅ carboxylate in one case and the water molecules represented by the O_{3w}, O_{4w} atoms are the mayor components (o.6 share in both cases). The minor components (O_{1w}, O_{3w} and O₃₇-C₇-O₃₈ respectively) are given in white. Thermal ellipsoids are at 35% probability level.

Table S1. Selected geometry parameters involving $\mu_3\text{-O/OH}$ bridges ^{a)}

O atom	d(Zr-O)/ Å		$\angle\text{Zr-O-Zr}$ /°	d(O...plane)/ Å	Assignment
	range	mean			
O2	2.092-2.130	2.106	114.4	0.505(5)	$\mu_3\text{-O}$
O4	2.062-2.120	2.086	117.3	0.347(5)	
O5	2.051-2.087	2.069	115.9	0.423(5)	
O7	2.046-2.083	2.062	116.3	0.400(5)	
O10	2.086-2.129	2.103	114.6	0.495(5)	
O12	2.062-2.116	2.084	117.2	0.351(5)	
O13	2.030-2.084	2.053	117.0	0.361(5)	
O15	2.074-2.081	2.076	115.6	0.441(5)	
O1	2.256-2.342	2.292	101.8	1.014(5)	$\mu_3\text{-OH}$
O3	2.246-2.347	2.283	102.4	0.996(5)	

O6	2.240-2.269	2.256	101.3	1.016(6)	
O8	2.254-2.304	2.274	101.1	1.028(6)	
O9	2.257-2.351	2.293	101.9	1.013(5)	
O11	2.249-2.314	2.276	102.5	0.988(5)	
O14	2.235-2.316	2.269	100.7	1.036(5)	
O16	2.241-2.284	2.265	101.5	1.014(5)	
O17 × 2	2.034-2.207	2.146	111.0	0.658(7)	
O18 × 2	2.035-2.212	2.147	110.3	0.685(6)	$\mu_3\text{-O}_{0.75}/(\text{OH})_{0.25}$
O19 × 2	2.196-2.236	2.219	106.6	0.838(8)	
O20 × 2	2.176-2.245	2.210	107.3	0.810(7)	$\mu_3\text{-O}_{0.5}/(\text{OH})_{0.5}$

^{a)} The e.s.d. values for Zr-O bond lengths and Zr-O-Z bond angles are 0.005-0.006 Å and 0.2-0.3°, respectively. The $\mu_3\text{-O}\cdots$ plane separation is the distance of the O-atom from the plane defined by the three coordinating Zr ions.

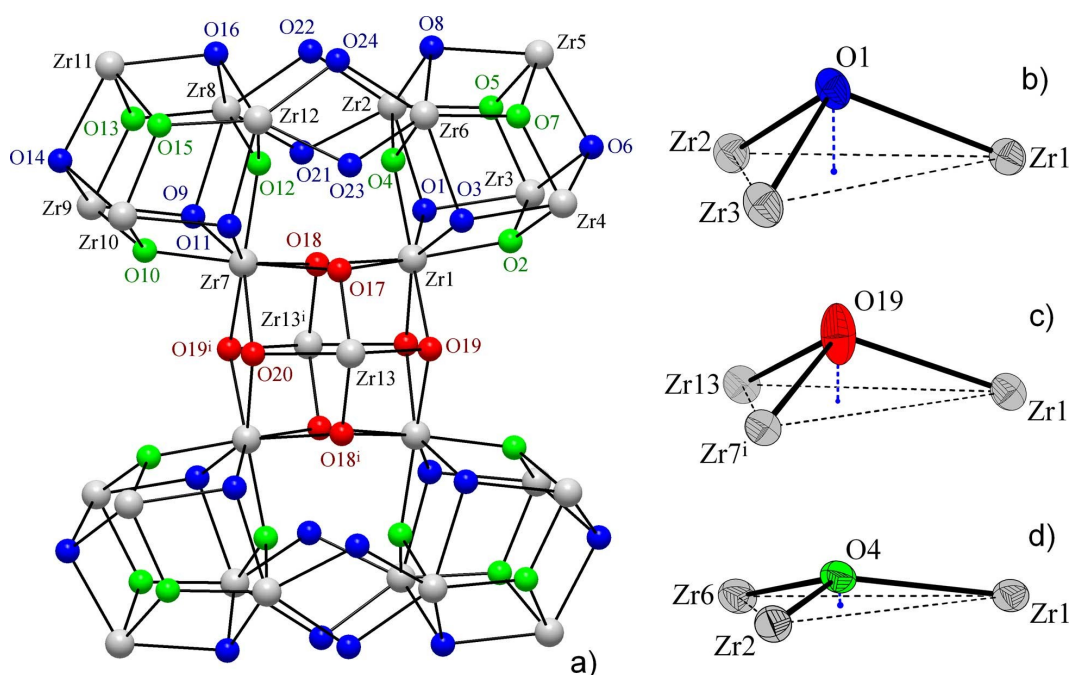


Fig. S3. a) Cluster-scheme featuring only the hydroxo- and oxo- ligands, with O-atoms of $\mu\text{-OH}$ and $\mu_3\text{-OH}$ ligands marked in blue, $\mu_3\text{-O}$ -atoms marked in green, and the averaged oxygen atom positions of the site sharing $\mu_3\text{-OH}$ / $\mu_3\text{-O}$ ligands marked in red. b-d) Typical geometries of the $\{\mu_3\text{-O(H)Zr}_3\}$ fragments with the same color notations of ligands as in the previous point. The fragments show decrease in the distance between the O-atom to the plane defined by the three coordinating metal ions. Note the high anisotropy of thermal motion of O-atom in the case of $\mu_3\text{-(OH/O)}$ site sharing [Symmetry code: (i) 1-x, 1-y, 1-z].

For the other twenty unique μ_3 -oxygen atoms (O1 to O20), the ranges of median Zr-O bond lengths (i.e. the averages of the three formed bonds), 2.034(5)-2.351(5) Å, and the median Zr-O-Zr bond angles, 99.2(2)-118.0(2)°, are much broader. However, three distinct types of the μ_3 -bridges are clearly distinguishable, featuring characteristic bond lengths and angles (Table S1).

Thus, for the group of eight μ_3 -O atoms, namely O2, O4, O5, O7, O10, O12, O13, O15, the Zr-O coordination bonds are the shortest (the range of the mean values are 2.030(5)-2.130(5) Å) and the Zr-O-Zr angles exceed 112° (114.4(2)-117.3(3)°), with the distance between the O atom to the plane of the three coordinating Zr ions being as low as 0.347(5)-0.505(5) Å.

Contrarily, the eight μ_3 -O atoms, namely O1, O3, O6, O8, O9, O11, O14, O16, adopt longer coordination bonds with average values in the range of 2.235(5)-2.351(5) Å and average bond angles below 105° (100.7(2)-102.5(2)°), while the $\{\text{Zr}_3\text{O}\}$ fragment deviate further from planar with separation between the O-atoms and the Zr_3 plane being in the range of 0.988(5)-1.036(5) Å.

The differences in average bond length and bonding angles allow the unambiguous assignment of the listed cases to μ_3 -O and μ_3 -OH ligands respectively. Exactly the same distribution of bond length and angles was reported, e.g. for $[\text{Zr}_{12}\text{O}_8(\text{OH})_8(\text{CH}_3\text{COO})_{24}] \cdot 4\text{CH}_3\text{COOH} \cdot 2\text{HCOOH} \cdot 0.5\text{H}_2\text{O}$ complex [6]. In the latter, the average Zr-O distances for μ_3 -O²⁻ are in the range of 2.047-2.091 Å, the average $\angle\text{Zr-O-Zr}$ angles are in 114.4-119.6°, and the O...plane distance is 0.400 Å. The same parameters for μ_3 -OH are: the average Zr-O is 2.219-2.374 Å, average $\angle\text{Zr-O-Zr}$ is 99.5-105.9°, and O...plane separation is 1.019 Å. Thus, each of the two crystallographically unique $[\text{Zr}_6(\mu_3\text{-O/OH})_8]$ 'corner' fragments of the Zr_{26} -cluster shows an already observed distribution of four μ_3 -O and four μ_3 -OH bridges, with alternation of the associated Zr_3 faces (Fig. S3).

For the central $[\text{Zr}_6(\mu_3\text{-O/OH})_8]$ fragment the situation is slightly more complicated. This fragment reside on a center of inversion and for all four unique μ_3 -O atoms, namely O17, O18, O19, O20, the bonding parameters (Zr-O, $\angle\text{Zr-O-Zr}$, O...plane, See Table S1) are intermediate between the values for the two above cases. This implies site-sharing of μ_3 -O and μ_3 -OH ligands. Such assignment agrees with the observed anisotropy of the oxygen atoms's ADPs in the direction perpendicular to the respective Zr_3 plane of the $\{\mu_3\text{-OZr}_3\}$ fragment (Fig. S3, c). Very similar situation, involving either the apparent average geometry or features of thermal motion, was observed for many examples of $\{\text{Zr}_6(\mu_3\text{-O/OH})_8\}$ carboxylates [7]. In the present case, contributions of μ_3 -O and μ_3 -OH groups are similarly unequal. Thus, for two symmetry related pairs of O17 and O18 atoms, deviation from the Zr_3 plane (0.658(7) and 0.685(6) Å) is appreciably smaller than for pairs of O19 and O20 atoms (0.838(8) and 0.810(7) Å). The latter pair exhibit also significantly narrower $\angle\text{Zr-O-Zr}$ angles and longer Zr-O bond lengths (Table S1). This suggests higher contribution of the μ_3 -O component to the site-sharing μ_3 -O/OH ligands represented by O17 and O18 atoms. It worth noting that O17 and O18 atoms are involved in very short O17...O23 and O18...O21 intracluster contacts with 2.657(8) Å and 2.651(8) Å length respectively, where the second atom in the pair belongs to the μ -OH ligand (Fig. S3), suggesting strong and highly directional [*i.e.*, $\angle\text{ZR8-O21...O18} = 102.0(5)^\circ$] intra-cluster hydrogen bonding. The above geometries allows to assign the O19 and O20 atoms to site-sharing μ_3 -O/OH ligands with 0.5/0.5 ratio, while for O17, O18 with 0.75/0.25 ratio, together constituting the central $\{\text{Zr}_6(\mu_3\text{-O})_5(\mu_3\text{-OH})_3(\text{COO})_4\}$ hexanuclear sub-cluster.

This scheme, incorporating 21 oxo and 27 hydroxo bridges in total, describe a neutral Zr_{26} cluster with a formula of $[\text{Zr}_{26}(\mu_3\text{-O})_{21}(\mu_3\text{-OH})_{19}(\mu\text{-OH})_8(\text{HCOO})_{35}(\text{H}_2\text{O})_5]$ and a structure, which has clear analogues on the level of $\{\text{Zr}_6\}$ sub-clusters with known compounds featuring the same fragment.

The highest residual electronic density peaks in the space between the loosely packed Zr_{26} cluster molecules were identified as solvate formic acid molecules. A set of geometry restraints and similarity restraints in the anisotropic thermal motion parameters (ADPs) were employed to improve the refinement stability. Three solvate formic acid molecules were treated

as disordered and refined with partial occupancy factors 0.60/0.40, 0.70/0.30 and 0.50 with fixed molecular geometry. Atoms of these groups were refined isotropically. The remaining electron density peaks in the $V = 780 \text{ \AA}^3$ per unit cell or 20.9% of the crystal volume were excluded from the refinement by the SQUEEZE/PLATON routine (132 e per unit cell; cf. with the ~31.7% of solvent accessible space calculated for the structure with all the solvent molecules removed from the inter-cluster space) [8, 9].

The final molecular composition is ascribed as a compromise with the TGA study (see below). The ~31.7% solvent accessible volume corresponds to 1180 \AA^3 pro unit cell, *i.e.* pro one Zr_{26} -cluster unit. Such volume could host up a few tens of water and formic acid molecules pro formula unit, however a part of it belongs to very narrow pores, not well suited for dense packing of even such a small molecule as water (the molecular volumes of H_2O and $HCOOH$ estimated from the density in the liquid phase are 29.9 and 62.7 \AA^3 / molecule respectively). Such high solvent contents were not confirmed, most probably due to partial solvent loss during drying.

The molecular graphics was computed using Diamond 3.2i [10].

Table S2 Crystal data and structure refinement for $[Zr_{26}O_{18}(OH)_{30}(HCOO)_{38}] \cdot 5(HCOOH) \cdot 2H_2O$, **1**.

	1
Empirical formula	$C_{40}H_{82}O_{133}Zr_{26}$
M_r /g mol ⁻¹	5062.77
T /K	180(2)
Wavelength / \AA	1.54186
Crystal system	Triclinic
Space group	$P\bar{1}$
a / \AA	11.4132(8)
b / \AA	18.7392(12)
c / \AA	19.1989(11)
α / $^\circ$	71.434(5)
β / $^\circ$	73.347(5)
γ / $^\circ$	81.818(5)
V / \AA^3	3723.3(4)
Z	1
Calc. density /g cm ⁻³	2.258
μ / mm ⁻¹	15.360
F(000)	2426

Crystal size /mm ³	0.04 × 0.02 × 0.02
θ range /°	4.025 to 70.953
Index ranges /hkl	[-13, 6]; [-21, 22]; [-23, 23]
Reflections collected (R _{int})	36620 (0.0451)
Independent reflections	14209
Completeness % to θ /°	99.2 % to 67.69
Data / restraints / parameters	14209 / 168 / 979
Goodness-of-fit	0.981
R[F ² >2σ(F ²)], wR2 ^{a)}	0.0561, 0.1533
R1, wR2 (all data)	0.0719, 0.1625
Largest diff. peak and hole, eÅ ⁻³	1.416 and -1.537
Solvent accessible volume []	20.9%
Electron count in the voids per formula unit	132

^{a)} Full-matrix least-square refinement on F² as implemented in SHELX-2014 [3]. $R1 = \frac{\sum ||F_o| - |F_c||}{\sum |F_o|}$; $wR2 = \frac{\{\sum[w(F_o^2 - F_c^2)]^2\}}{\sum[w(F_o^2)]}^{1/2}$ where $w^{-1} = [\sigma^2(F_o^2) + (aP)^2 + bP]$, $P = [2F_c^2 + \text{Max}(F_o^2, 0)] / 3$, a and b are refined parameters; $\text{Goof} = \{\sum[w(F_o^2 - F_c^2)^2] / (n-p)\}^{1/2}$.

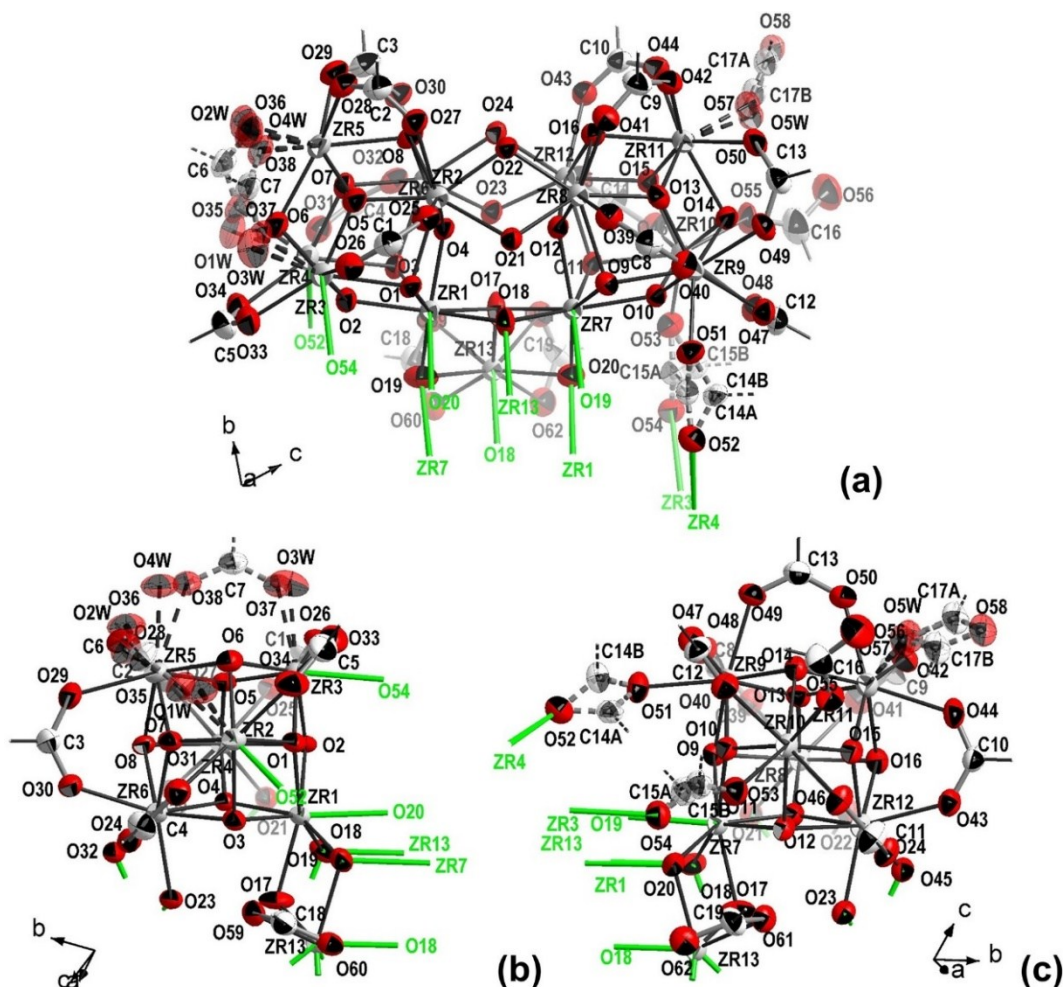


Fig. S4. ORTEP-style drawing of **1**; broken-off bonds are shown by green
 (a) The asymmetric unit.
 (b, c) The Zr₆-subunits depicted separately for better visibility of the connectivity.

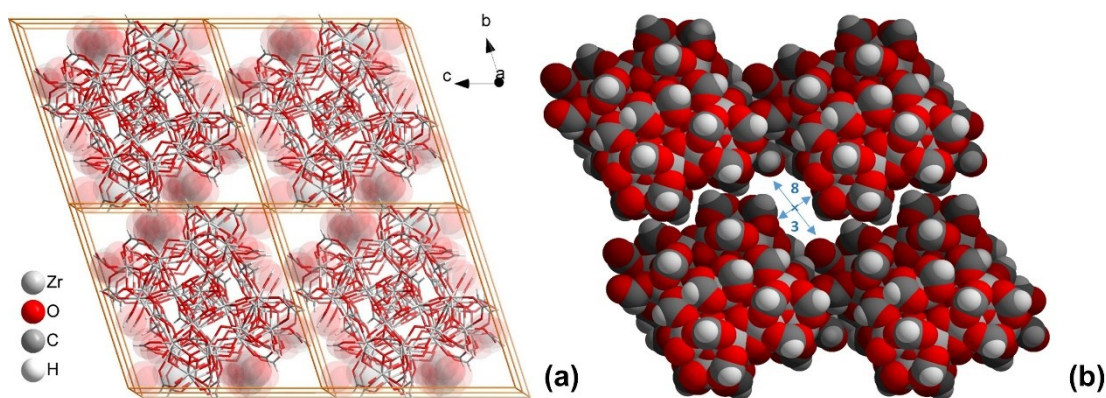


Fig. S5. The packing of the Zr₂₆-clusters in **1** (the unit cells are shown in orange).
 (a) The cluster molecules are shown in wireframe representation, while the refined solvent molecules in semitransparent space-filling representation.
 (b) The cluster molecules are shown only; space-filling representation is used. The thorough-pore vdW dimension is ~8×3 Å (centerline runs through the cell-

origin along *c*-axis).

3. PXRD

The diffractogram (Fig. S6) was recorded using a Bruker D2 Phaser diffractometer in reflective mode, equipped with a Bragg-Brentano goniometer, graphite monochromator (Cu $K\alpha$, $\lambda = 1.5418 \text{ \AA}$; 30 kV, 10 mA source) and Lynxeye 1D detector. The measurement was performed at room temperature with 0.05° steps on a freshly prepared sample, amply wetted with mother solution and placed on a zero-background Si single crystal plate sampleholder. Drying of the sample leads quickly to partial deterioration of the sample's quality. While application of cover foil decreased the quality of the sample substantially, a short and fast measurement with a relatively small sampling rate was performed, ensuring that the sample remains wet (wetting the sample also mostly eliminates the possible problem of preferred orientation). Despite of the relatively low number of data points collected, the near perfect correspondence of the experimental and simulated patterns (generated by Mercury 3.3.1. software, CCDC) is evident.

It is worth noting the importance of performing the measurement on a freshly synthesized sample. The PXRD patterns change noticeably after a few days of storage of the sample in the mother-solution at room temperature (even if the ensuing patterns were all quite close, precise overlapping was not possible anymore). It was also observed that similar variation of quality might occur in repeated syntheses. We interpreted those variations rather as change in quality of the material than as significant presence of phase impurities (the main arguments are the closeness of the patterns and the observance of near perfect overlap in one case).

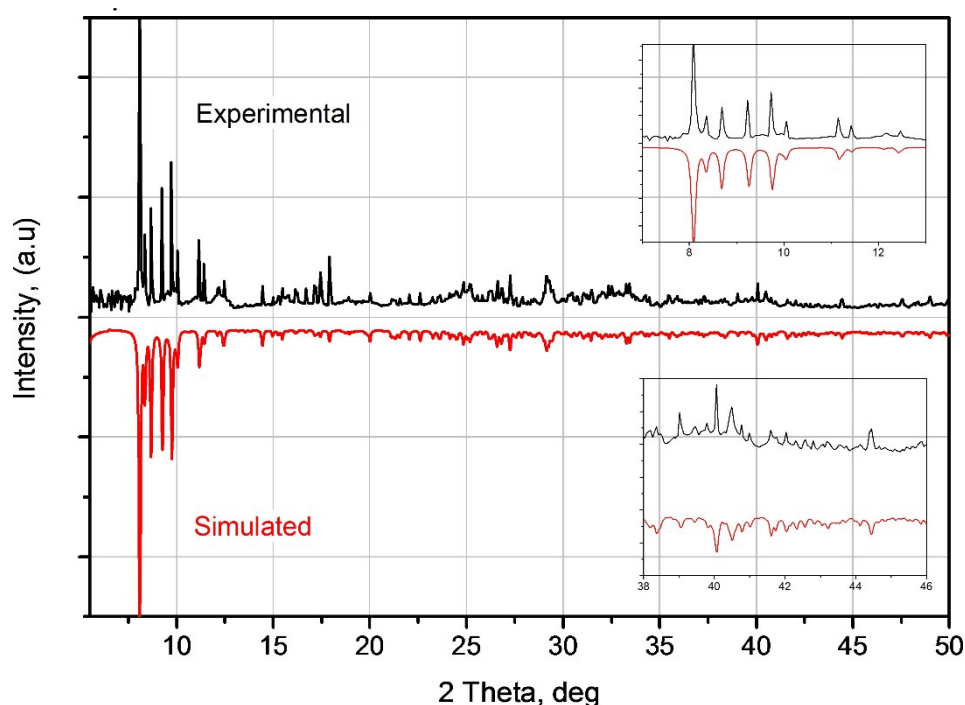


Fig. S6. Comparison of the experimental PXRD pattern of as-synthesized **1** with the simulated pattern calculated from SCXRD data.

4. TGA

Thermogravimetric analysis data was collected on a Netzsch TG 209F3 instrument using corundum sampleholder under N₂ gas stream (10 ml min⁻¹) at 10 °C min⁻¹ heating rate.

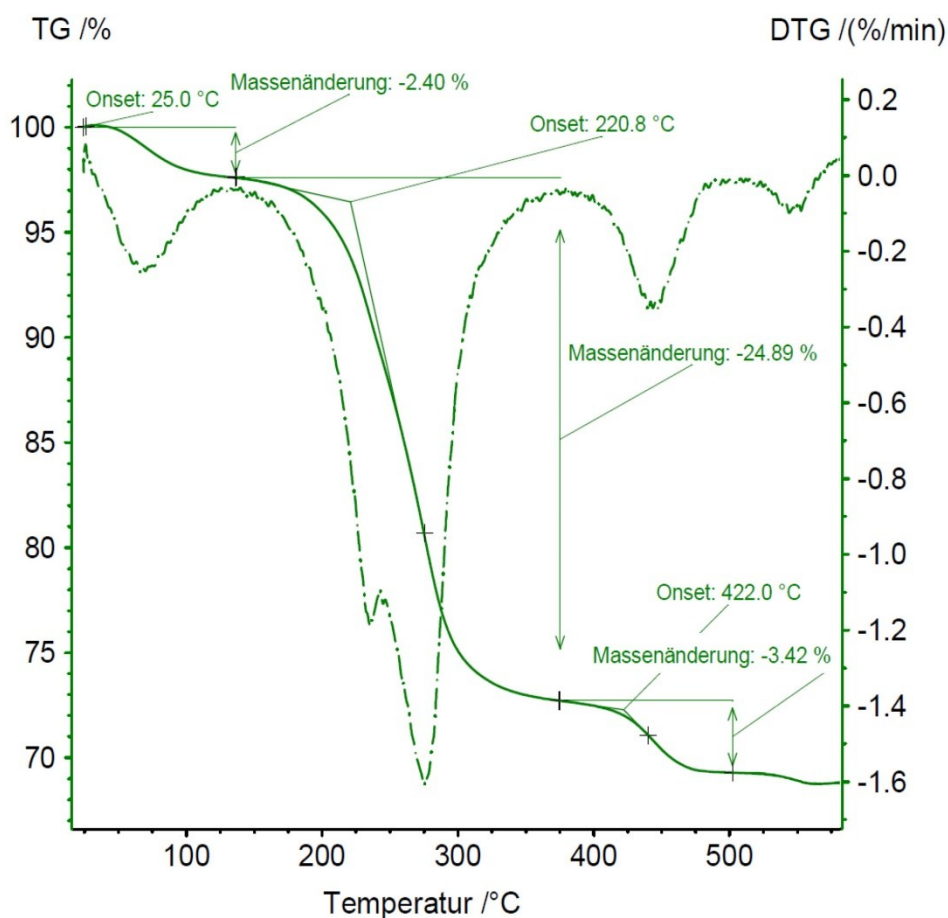


Fig. S7 Thermogravimetric analysis (TGA) of 1. The $m(T)$ dependence is given by a solid line, while the differential $dm/dT(T)$ dependence in a dot-and-dash line.

There are three weight-loss steps: 2.4% at r.t. - ~150 °C, 24.9% at ~150 – 380 °C and ~4.0% at 380 – 550 °C, in total accounting for 31.3% (Fig S7).

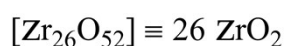
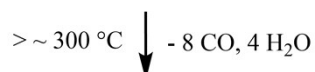
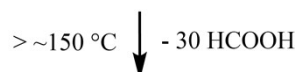
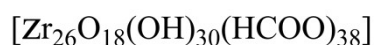
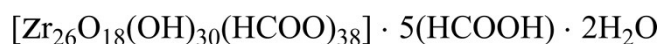


Fig. S8 Plausible decomposition steps for **1** under the TGA conditions.

The proposed decomposition scheme is given in Fig. S8 with the anticipated temperatures. Complete release of water and e.g. formic acid with comparable boiling point from moderately hydrophilic microporous compound should mostly take place at temperatures typically below 150 °C (strongly bound water could be to some small extent retained even at that temperature). Regarding the second step, it is known as a method of defect generation in UiO-66 type compounds that trifluoroacetate could be released in a form of trifluoroacetic acid at temperatures around 250 °C using the -OH groups as the source of proton [11]. Further increase of temperature necessarily leads to decomposition of the remaining formates to carbon monoxide, water and oxo-anions, resulting in formation of zirconium oxide. It is worth to stress that the steps, especially the second and the third one are surmised as not being rigorously separated.

The calculated weight of the residues after the proposed steps are 94.8%, 68.0% and 62.2%. The observed weight of the residue after the third step is 68.7%, which is somewhat more than the predicted value. It points out on the impurity of the isolated phase and probably on a significant presence of hydrated zirconium oxides, which do not contain formates / formic acid.

5. FT-IR spectroscopy

The FT-IR spectra (Fig. S9) were collected by a Bruker Tensor 37 system equipped with an ATR unit (Platinum ATR-QL, diamond) in the 4000-550 cm^{-1} range with a 2 cm^{-1} resolution (32 scans per measurement). Peak intensities were designated as: s – strong, m – medium, w – weak, br – broad, sh – shoulder, v- ‘very’ prefix:

FT-IR (ATR), $\tilde{\nu}$, cm^{-1} : 3398 (vw, b), 2866 (vw), 1567 (vs), 1467 (w), 1389 (w), 1361 (vs), 1019 (w), 916 (w), 805 (w), 760 (m), 704 (w), 644 (vs), 566 (w) (the data is given for a scaled-up synthesis of **1** after its drying until constant weight).

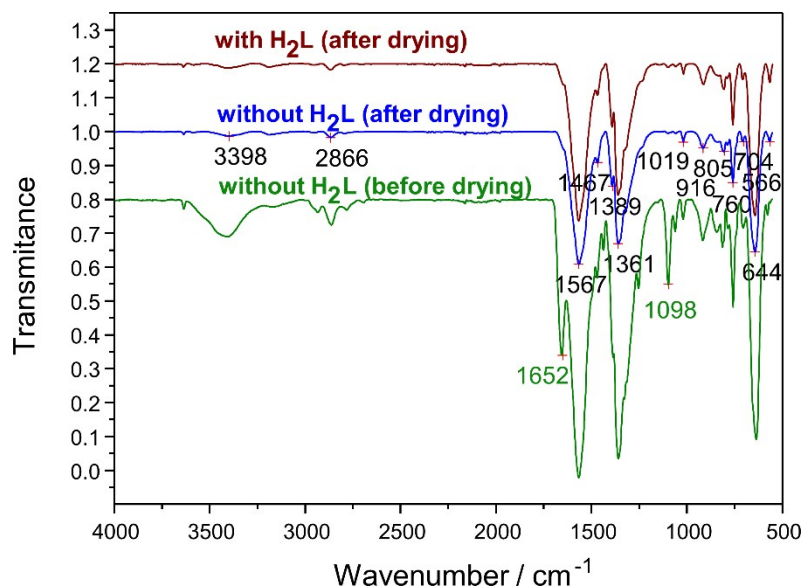


Fig. S9. IR(ATR) spectrum of **1**. The IR spectra of the compounds synthesized in the presence of 1,3-di(4-carboxyphenyl)adamantane, H₂L, or without it are nearly identical. Note the disappearance of the peaks characteristic to DMF, ~1650 and 1100 cm^{-1} , upon drying.

6. ^1H NMR spectrum of **1** after digestion

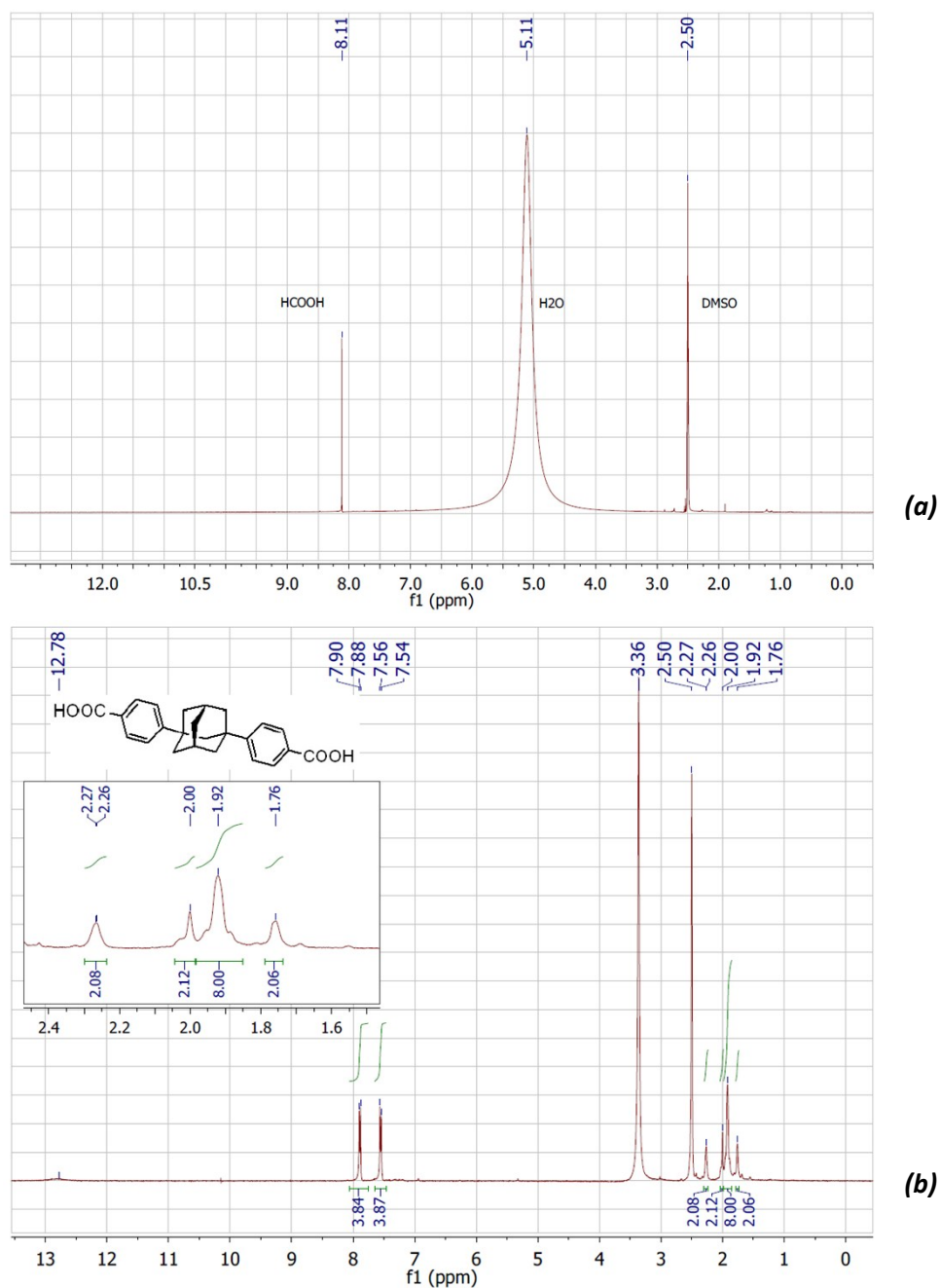


Fig. S10. a) ^1H NMR spectrum of **1** synthesized in the presence of H₂L after digestion b) ^1H NMR of H₂L for comparison.

A sample of **1** prepared in presence of 1,3-di-(4-carboxyphenyl)-adamantane, H₂L was thoroughly washed with DMF in order to remove the non-bound H₂L, and after drying in air until permanent weight, was digested in a mixture of 30 μL HF (40% solution in H₂O) and 570 μL of DMSO- d_6 (Fig. S10a; 300 MHz). The ^1H NMR spectrum of the digested sample (Fig. S10a) clearly indicates that no ligand incorporation occurred (see Fig. S10b for the spectrum of the pure ligand; DMSO- d_6 , 200 MHz).

7. Gas adsorption studies

The preliminary N₂ adsorption isotherms were collected using a Quantachrome Nova-, while the final adsorption data for N₂, CO₂ and H₂ by Micromeritics ASAP 2020 automatic gas sorption analyzers. The control equilibration time, i.e. the time between subsequent data points, used for checking whether the equilibration is complete, was set to 30 s for the high quality measurements on the ASAP 2020 (this value is ~2-3 times more than it is used for typical measurements on a material with large or medium pores). In this way it was ensured that the hysteresis loop is not an artifact of the measurement). The minimum absolute surface area measurable with reasonable precision on the ASAP 2020 is approx. 5 m², which was accounted for adjustment of the used sample weights.

The N₂ data was measured repeatedly, with one pair of cross-check measurements using both instruments. The used gases (He, N₂, CO₂, H₂) were of ultra-high purity (UHP, grade 5.0, 99.999% or better) and the STP volumes are given according to the NIST standards (293.15 K, 101.325 kPa). Helium gas was used for the determination of the cold and warm free space of the sample tubes. The N₂ and H₂ adsorption isotherms were measured at 77 K (liq.-N₂ bath), while the CO₂ adsorption isotherm at 273.15 K using an ice-water isothermal bath.

A freshly prepared sample was filtered-off from the mother solution, washed 3 times with DMF and then soaked for a short time in acetone (<30 min. The short soaking time was a most probably unnecessary precaution against the deterioration of the sample's quality. Longer times might gave better results, but most probably by a small margin only). The soaking in acetone was repeated once and the collected sample was thereafter transferred in LEICA EM CPD300 supercritical CO₂ drier. 99 standard cycles were performed. ~100-110 mg of the dried and degassed material was used for the subsequent degassing and adsorption measurements.

A cursory optimization of the degassing temperature was done by performing comparative measurement after degassing at 100, 150, 190, 240 °C (The same sample was used and the degassing was sequentially done at higher temperature after each measurement). Degassing at 150 °C or below yielded materials with surface areas not exceeding 32 m² g⁻¹, while the degassing at 240 °C afforded a material with negligible porosity. Thus, the optimum was found to be around 190 °C). The samples (~110-120 mg) were activated via heating under ~10⁻³ mbar vacuum in the case of Quantachrome Nova or ~10⁻⁵ mbar in the case of ASAP 2020 at 190 °C during 16-24 h.

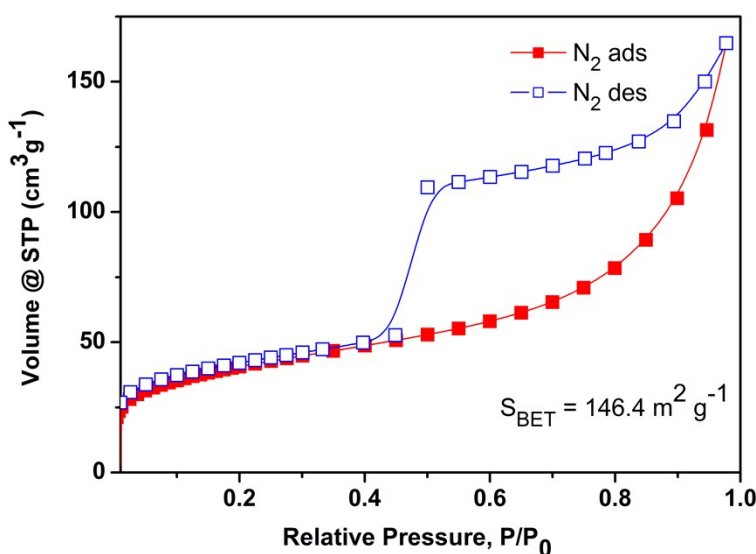


Fig. S11. N₂ adsorption isotherm for 1' ₄₆₃ measured on 77K on the sample

obtained by degassing of **1** at 463 K.

An $S_{\text{BET}} = 146 \text{ m}^2 \text{ g}^{-1}$ Brunauer–Emmett–Teller (BET) surface area was found (repeated N_2 -only measurements on the same batch, but dried and degassed separately, gave 153 and $156 \text{ m}^2 \text{ g}^{-1}$). The adsorption isotherm (Fig. S11) demonstrates a strong hysteresis (H2-type) with a distinct shape, having an abrupt desorption branch contrasting with the steady adsorption branch. The shape of the hysteresis is characteristic for capillary condensation of gases in mesoporous materials, particularly in the presence of ‘ink-bottle’ pores.[¹²] The latter term is standard and denotes ‘bottle-necked’ pores, with effective entrance diameter of the pore significantly smaller than the effective inner-diameter. Simulations of the adsorption isotherm shapes see for example in ref. [¹³].

The adsorption isotherms of CO_2 at 273K and H_2 at 77K are shown on Fig. 12 and Fig. 13 respectively. Both isotherms demonstrate narrow hysteresis loops over the whole measurement range, most probably reflecting the kinetic hindrances of desorption from the narrowest pores (the molecules of both gases have smaller equivalent kinetic diameters than N_2 and could reach areas associated with especially narrow pores with increased heats of adsorption). The observed values are in the standard range, if one takes in account the surface area. Thus, the so called ‘Chahine’s rule’ [¹⁴] establishes an excess adsorption of 0.021 mg m^{-2} at 1 bar and 77 K, while **1**'₄₆₃ demonstrates a value of 0.017 mg m^{-2} (at 1 bar and the observed adsorption the difference between the total and excess adsorption is only a few percent).

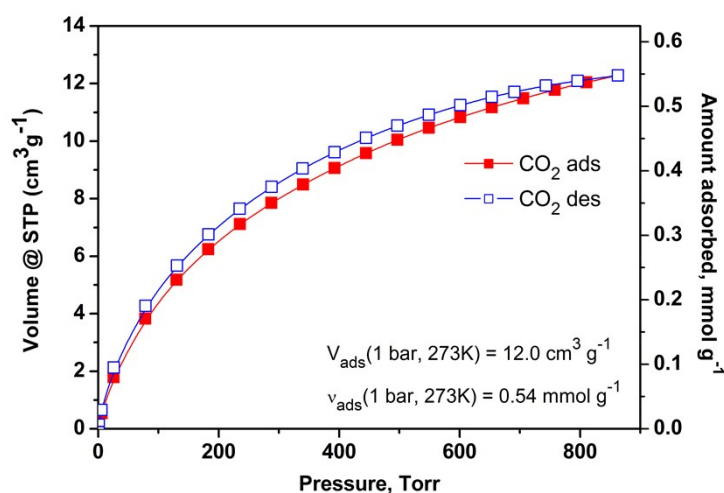


Fig. S12. CO_2 adsorption isotherm for **1**'₄₆₃, measured at 273 K.

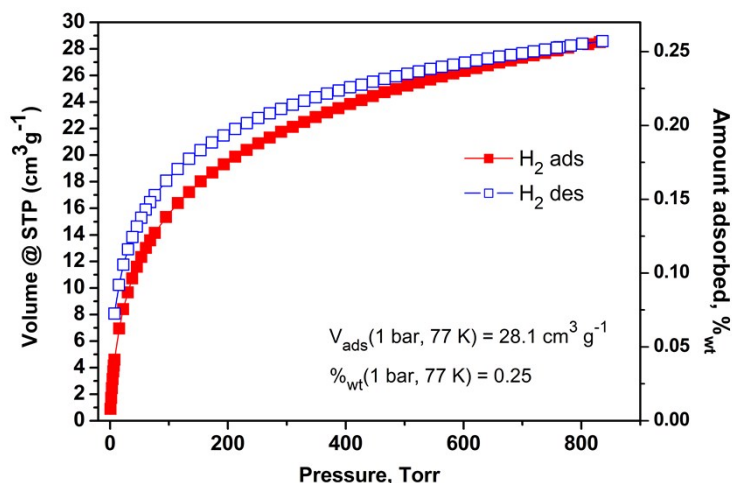


Fig. S13. H₂ adsorption isotherm for 1'463, measured at 77 K.

References

- ¹ T. Zhao, C. Heering, I. Boldog, K. V. Domasevitch, and C. Janiak, *CrystEngComm*, 2017, **19**, 776–780.
- ² STOE & Cie GmbH (2016). X-Area 1.76, software package for collecting single-crystal data on STOE area-detector diffractometers, for image processing, scaling reflection intensities and for outlier rejection; Darmstadt, Germany.
- ³ STOE & Cie. *X-SHAPE*. Revision 1.06. Stoe & Cie GmbH, Darmstadt, Germany, 1999; Stoe & Cie. *X-RED*. Version 1.22. Stoe & Cie GmbH, Darmstadt, Germany, 2001.
- ⁴ G. M. Sheldrick, *Acta Crystallogr.* **2008**, *A64*, 112-122. G. M. Sheldrick, *Acta Crystallogr.* **2015**, *C71*, 3-8.
- ⁵ P. Ji, K. Manna, Z. Lin, X. Feng, A. Urban, Y. Song, and W. Lin, *J. Am. Chem. Soc.* **2017**, *139*, 7004–7011.
- ⁶ A.A. Bezrukov, K.W. Törnroos, E. Le Roux and P. D. C. Dietzel, *Chem. Commun.*, **2018**, *54*, 2735-2738.
- ⁷ P. Piszczek A. Radtke, A. Grodzicki, A. Wojtczak, J. Chojnacki, *Polyhedron*, **2007**, *26*, 679–685.
- ⁸ A. L. Spek, *Acta Crystallogr. Sect. C Struct. Chem.*, 2015, **71**, 9–18.
- ⁹ A. L. Spek, *Acta Crystallogr. Sect. D Biol. Crystallogr.*, 2009, **65**, 148–155.
- ¹⁰ H. Putz and K. Brandenburg, *Diam. 3.2, Cryst. Impact; Kreuzherrenstr. 102, 53227 Bonn, Ger.*, 2012.
- ¹¹ F. Vermoortele, B. Bueken, G. Le Bars, B. Van De Voorde, M. Vandichel, K. Houthoofd, A. Vimont, M. Daturi, M. Waroquier, V. Van Speybroeck, C. Kirschhock, and D. E. De Vos, *J. Am. Chem. Soc.*, 2013, **135**, 11465–11468.
- ¹² S. J. Gregg and K. S. W. Sing, *Adsorption, Surface Area, and Porosity*, Academic, New York, 2nd ed, 1982, pp. 303.
- ¹³ Y. Zeng, C. Fan, D. D. Do, and D. Nicholson, *Ind. Eng. Chem. Res.*, 2014, **53**, 15467–15474.
- ¹⁴ B. Panella, M. Hirscher, and S. Roth, *Carbon N. Y.*, 2005, **43**, 2209–2214.